ROYAL SOCIETY OF CHEMISTRY

PAPER

Dual-sized NiFe layered double hydroxides *in situ* grown on oxygen-decorated self-dispersal nanocarbon as enhanced water oxidation catalysts†

Xiaolin Zhu,‡[ab] Cheng Tang,‡[a] Hao-Fan Wang,[a] Qiang Zhang,*[a] Chaohe Yang[b] and Fei Wei[a]

The oxygen evolution reaction (OER) is extensively involved in various sustainable energy processes and systems, such as water splitting, fuel cells, and metal–air batteries. Towards superior OER performance, the wise integration of transition metal compounds with nanocarbon materials is a promising strategy. Herein, a mildly oxidized graphene/single-walled carbon nanotube hybrid was introduced to regulate and control the hybridization of nickel–iron layered double hydroxides into a nanocarbon scaffold. The oxygen functionalities and defects anchored the nucleation and *in situ* growth of dual-sized layered double hydroxides, leading to a hierarchical porous structure for smooth mass diffusion, intimate interfaces for rapid charge transfer, and efficiently utilized active sites. Attributed to the synergy of individual components and the unique structural features, the as-fabricated composites exhibited superior OER performance with a small onset overpotential (*ca.* 240 mV), a low overpotential required for 10 mA cm^{-2} (*ca.* 350 mV), and a decreased Tafel slope (*ca.* 54 mV dec^{-1}) in 0.10 M KOH. This work provides a brilliant catalyst for water oxidation and more importantly, opens up new avenues for preparing nanocarbon-based multi-functional composites applicable in heterogeneous catalysis, energy conversion and storage, and so on.

1. Introduction

Growing consumption of fossil fuels and increasing concern about environmental pollution stimulate the pursuit of alternative sustainable energy solutions.[1–3] The oxygen evolution reaction (OER) is an important half-reaction of water splitting towards clean hydrogen-energy, and also highly involved in various sustainable energy conversion and storage systems, such as fuel cells and metal-air batteries.[4,5] However, this multi-electron process ($4OH^- \rightarrow O_2 + 2H_2O + 4e^-$, in alkaline solution) is kinetically sluggish, which calls for an efficient catalyst to expedite the reaction and reduce the high overpotential.[6,7] Precious metal oxides (*e.g.* IrO_2 and RuO_2) are the state-of-the-art OER electrocatalysts typically used in acidic solution, but

their practical applications are severely limited by their scarcity, high cost, and poor stability.[8,9] Recently, transition metal (Ni, Co, Fe, Mn, *etc.*) compounds[10–21] with excellent catalytic activity in base, high abundance, and eco-friendly character have appeared to be a family of outstanding alternatives. In particular, NiFe layered double hydroxides (LDHs),[22–28] with the advantages of incorporating Fe into α-Ni(OH)$_2$/γ-NiOOH lattices towards a lower overpotential and a layered structure allowing anion intercalation to obtain bulk redox activity, are widely recognized as the most promising substitutes.
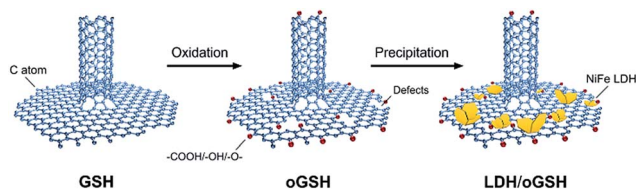
One of the major issues faced with NiFe LDHs is low electrical conductivity, which seriously restricts the electron transport and consequently degrades the electrochemical performance.[25,29] Various nanocarbon materials, such as carbon nanotubes (CNTs),[29] graphene,[30–35] and carbon quantum dots,[36] have been hybridized with NiFe LDHs to enhance the electron-transfer properties and resolve this challenge recently. However, as for the one-dimensional CNTs and two-dimensional graphene, they are both inclined to aggregate or stack together due to the intense van der Waals forces, thereby leading to a poor structural hierarchy and hindering the electrolyte-access and gas-release processes. While for the zero-dimensional carbon quantum dots, an interconnected electrically conductive network is lacking. Moreover, the NiFe LDH sheets always

24540 | *J. Mater. Chem. A*, 2015, **3**, 24540–24546

This journal is © The Royal Society of Chemistry 2015

Scheme 1 Synthesis of LDH/oGSH electrocatalysts with a dual-sized distribution of LDH plates through moderate oxidation and *in situ* co-precipitation.

randomly pack and bank on these nanocarbon substrates, which substantially reduces the utilization efficiency of the active sites.[33] Therefore, the fine hybridization of NiFe LDHs with nanocarbon materials to obtain a hierarchical structure with an interconnected electron-transfer pathway, fully exposed active sites, and intimate interfacial interactions still remains a great challenge towards superior OER catalysis.

The chemical vapor deposition (CVD) fabricated graphene/single-walled CNT hybrids (GSHs), with the superiorities of a three-dimensional (3D) self-dispersal structure, an interconnected electronic conductive network, and a strongly coupled C–C bonding interface, are quite a promising alternative to overcome the shortcomings of graphene and CNTs.[37,38] The reason for selecting single-walled CNTs and single-layer graphene as building blocks to fabricate GSHs is that they are considered as the high end for nanocarbon technology due to their much better intrinsic properties than those of multi-walled CNTs and multi-layer graphene, such as a larger specific surface area, lower defect density, and tunable electronic characteristics according to their edge/chirality.[39,40] In this regard, we introduced the novel GSHs as the scaffolds to modulate the *in situ* growth and hybridization, leading to a dual-sized distribution, uniform dispersion, and strongly coupled interaction of NiFe LDHs on the nanocarbon substrates. As illustrated in Scheme 1, the mildly oxidized GSHs (oGSHs) with abundant functionalities and moderate defects anchored the nucleation and *in situ* growth of NiFe LDHs, giving rise to hierarchical porous structures for smooth mass diffusion, intimate interfaces for rapid electron transfer, and efficiently utilized active sites. Consequently, the as-obtained LDH/oGSH electrocatalyst was demonstrated to exhibit superb OER performance with a high reactivity, low overpotential, and long durability in alkaline solution.

2. Results and discussion

Structure of the LDH/oGSH electrocatalyst

The GSHs were fabricated *via* facile CVD growth using calcined and reduced FeMgAl LDHs as catalysts.[37,41,42] The as-obtained GSHs exhibited a 3D self-dispersible feature. The CNTs were anchored on and sandwiched between the graphene sheets, preventing the stacking of graphene or aggregation of CNTs (Fig. S1a†). An intimate C–C bonding connection[37] was also observed between the graphene and CNTs (Fig. S1c†). After mild oxidization following a modified Hummers' method,[43]

moderate defects and oxygen-containing functional groups were introduced onto the surface of GSHs. The resultant oGSH material, with a 3D porous framework, interconnected electronic conductive network, and tunable surface chemistry, afforded a promising and effective scaffold for the hybridization of NiFe LDHs *via* a urea-assisted and oGSH-substrated co-precipitation procedure (Scheme 1). It was supposed that, during the precipitation process, both the oxygen-containing groups and the topological defects of oGSHs induced by oxidation treatment tended to adsorb and anchor the metal nitrate seeds (with a molar ratio of Ni/Fe = 3.0), and then the *in situ* nucleation and growth led to uniform NiFe LDH decoration on the nanocarbon scaffolds.

The scanning electron microscopy (SEM) image of the as-obtained LDH/oGSH composites (Fig. S2a†) indicated that the *in situ* grown NiFe LDH flakes were separately and uniformly decorated on the oxygen-decorated carbon frameworks, with a lateral size of *ca.* 100 nm, predominantly. The transmission electron microscopy (TEM) image further indicated that the typical *ca.* 100 nm NiFe LDHs were dispersed over the porous carbon scaffolds without any obvious aggregation (Fig. 1a) and attached onto the nanocarbon surface. Additionally, a large number of LDH nanoplates with a size of *ca.* 5 nm were also observed on the oGSH substrate, which were embedded into the encircling graphitic layers (Fig. 1b–c). The novel dual-sized distribution of the as-fabricated NiFe LDHs is notable and expected to be beneficial for superior electrocatalytic performances, which will be discussed below.

The elemental composition of the LDH/oGSH electrocatalyst was measured by X-ray photoelectron spectroscopy (XPS), and the atomic ratio of Ni to Fe was determined to be 2.9 (Fig. 1d), which was close to the ratio of their nitrite precursors. Furthermore, the X-ray diffraction (XRD) patterns (Fig. 1e) exhibited a group of hydrotalcite-like characteristic (003), (006), (012), and (110) peaks, demonstrating that the NiFe LDH phase was well crystallized in the composites. And the hexagonal appearance of NiFe LDHs with a fringe spacing of 0.25 nm

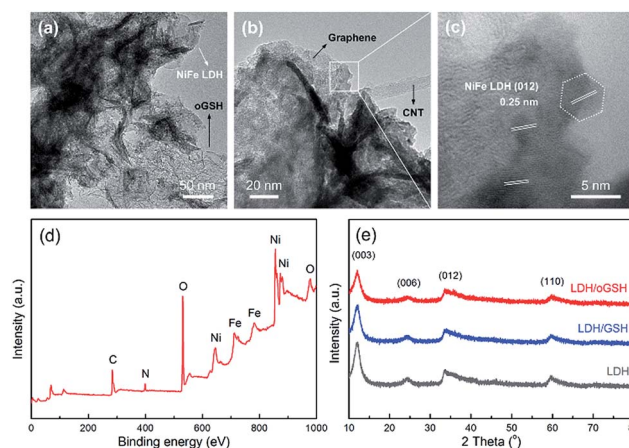

Fig. 1 Characterization of LDH/oGSH electrocatalysts. (a and b) TEM and (c) high resolution TEM images of the LDH/oGSH catalyst. (d) XPS survey spectrum of the LDH/oGSH catalyst. (e) XRD patterns of LDH/oGSH, LDH/GSH, and bulk LDH catalysts.

(Fig. 1c) was in accordance with the (012) lattice plane. All these results suggested the successful fabrication of a novel LDH/oGSH composite, in which dual-sized NiFe LDHs were uniformly incorporated and strongly coupled with the self-dispersal nanocarbon substrate.

Using the pristine GSHs instead of oGSHs, a counterpart complex (LDH/GSH) was prepared under otherwise identical conditions. Notably, in the case of LDH/GSH, NiFe LDH plates tended to aggregate together and stack disorderly on the GSH substrate (Fig. S2b†), remarkably reducing the accessibility of the active sites. Through comparison with the uniform decoration of hierarchically structured LDHs into the oGSH framework, a defect-anchored mechanism for NiFe LDH nucleation and growth in the LDH/oGSH hybrid was concluded. A physical mixture of bulk NiFe LDHs and oGSHs (LDH + oGSH) was also prepared for comparison (Fig. S2c and d†). The mass ratio of LDHs and carbon was revealed to be similar for all composites according to the thermogravimetric analysis (TGA) results (Fig. S3†). The as-prepared LDH + oGSH mixture appeared to be quite different from the *in situ* grown samples. The NiFe LDH sheets mostly aggregated into small clusters, which were packed randomly on the oGSH underlayer, and even peeled off from the nanocarbon matrix (Fig. S2d†), substantially weakening the interfacial junctions between two individual constituents and undermining the interconnected electro-conductive network. According to the pore size distributions characterized by N_2 adsorption–desorption isotherms (Fig. S4†), the mesopores ranging from 5 to 10 nm of the physical mixture were less decreased than the *in situ* grown composites, indicating fewer occupation and poor attachment of NiFe LDHs on the oGSH substrate.

Oxygen evolution catalytic performance

OER electrocatalytic performance of the *in situ* grown composites, their individual components, and the physical mixtures was comparatively tested in O_2-saturated 0.10 M KOH solution on a three-electrode system with a loading of *ca.* 0.25 mg cm^{-2}, and the results are shown in Fig. 2.

Fig. 2a presents the *i–R* compensated linear sweep voltammetry (LSV) curves obtained at a scan rate of 10 mV s^{-1}. The OER current density is directly related to the water oxidation process, thereby reflecting the catalyst activity. The overpotential needed to achieve a current density of 10 mA cm^{-2} (η_{10}), which corresponds to 10% efficient solar water-splitting device, is also an important parameter for OER catalyst evaluation.[44] As for both criteria, LDH/oGSH outperformed all individual components and physical mixtures with the highest current density and lowest η_{10}, substantially demonstrating the superiorities of the novel composite resulted from synergistic and coupling effects. Moreover, the performance of LDH/oGSH was improved in 1.0 M KOH electrolyte, where both a higher OER activity and lower η_{10} (reduced by *ca.* 80 mV) were obtained (Fig. S5a†). Here, it is notable that a comparable reactivity to that of LDHs was obtained for the GSH electrocatalyst, due to the oxygen functionalities in carbon materials, especially ketonic C=O groups, which were found to play crucial roles in
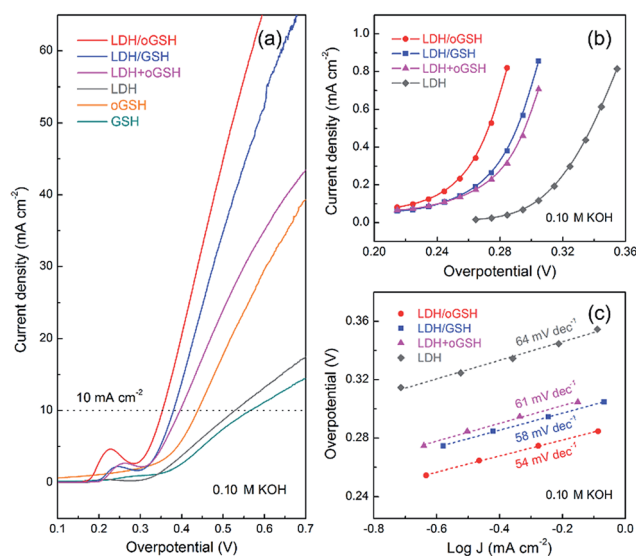

Fig. 2 OER performances of LDH/oGSH and control samples in 0.10 M KOH electrolyte. (a) *i–R* compensated LSV curves obtained at a scan rate of 10 mV s^{-1} and a loading of 0.25 mg cm^{-2}. (b) Voltammetric curves obtained by the chronoamperometric method and (c) the corresponding Tafel plots.

catalyzing OER by altering the electronic structure of surrounding carbon atoms and facilitating the adsorption of OER intermediates.[45] And the activity was further boosted after mild oxidation. Resulting from the unique 3D self-dispersal structural feature, a higher OER activity than that of both graphene and CNT samples was also detected for GSHs (Fig. S6†).

In the LSV curves of the samples containing NiFe LDHs, a redox peak around 0.2 V overpotential was detected (Fig. 2a), which was assigned to the Ni^{2+}/Ni^{3+} redox process. The peak areas varied obviously for different samples. It is noteworthy that the larger the peak area, the higher the OER reactivity. Taking LDH/oGSH for example, the highest redox peak suggested the most charge transferred relating to Ni^{2+}/Ni^{3+} transformation, and the resultant (Ni, Fe)OOH phase was believed to be crucial for the OER activity of NiFe LDHs,[46] thereby endowing this composite with the best catalytic performance. However, there is still controversy on the role of Fe^{3+} in the OER reactivity. Some studies proposed that the incorporation of Fe^{3+} activated the surrounding Ni^{3+} with a partial-charge-transfer effect, further altering their local environment and electronic structure towards an increased activity of Ni^{3+} sites.[14,47] While other studies supposed that the Fe^{3+} impurity adsorbed the OER intermediates preferentially, thereby generating more favorable active sites than Ni^{3+} species.[46] In this work, we fabricated the NiFe LDHs with the same Ni/Fe ratio in all catalyst samples, which afforded highly active Ni^{3+} species for water oxidation.

Notably, the overpotential range of catalyst oxidation was overlapped with that of oxygen evolution, making it difficult to determine the onset potential and Tafel slope. To decouple these two reactions, a chronoamperometric testing method has been employed to achieve sole OER currents at a series of potentials slightly above the redox peak (see the Experimental section for details). The onset overpotential (η_{onset}) of LDH/

24542 | *J. Mater. Chem. A*, 2015, **3**, 24540–24546

This journal is © The Royal Society of Chemistry 2015

oGSH was determined to be 0.24 V, comparable to that of LDH/GSH and LDH + oGSH around 0.26 V, but far less than bulk NiFe LDHs with a η_{onset} of 0.31 V (Fig. 2b).

The corresponding Tafel plots in Fig. 2c revealed that LDH/oGSH also exhibited the lowest Tafel slope of 54 mV dec^{-1}, much lower than those of LDH/GSH (58 mV dec^{-1}), LDH + oGSH (61 mV dec^{-1}), and bulk NiFe LDH (64 mV dec^{-1}). Such a small Tafel slope of LDH/oGSH implied a significantly boosted current density at higher overpotential and a lower electrochemical polarization phenomenon. Compared with some recently reported NiFe-based electrocatalysts, the LDH/oGSH exhibited a low onset potential among the best results in the range of 220 to 250 mV, and also delivered a competitive kinetics with a Tafel slope approaching 50 mV dec^{-1} (Table S1†). With further optimization of NiFe LDH phases and regulation of the active phase/carbon ratio, the performance of this novel hybrid is expected to be promising for practical applications.

The faradaic efficiency of the LDH/oGSH catalyst for OER was further determined by using a rotating ring disk electrode (RRDE), which enabled the study of OER at a central disk electrode and the collection of produced O$_2$ at a surrounding Pt ring electrode (Fig. S7†). With the increase of applied overpotential on the LDH/oGSH coated disk electrode, the as-determined faradaic efficiency decreased gradually from *ca.* 96 to 69% (Fig. S7†), due to the generation of O$_2$ bubbles and only the reduction of dissolved O$_2$ on the ring electrode surface. Therefore, 96% faradaic efficiency obtained at a disk current density of *ca.* 1.0 mA cm^{-2}, which was large enough to generate fully dissolved O$_2$ without forming O$_2$ bubbles,[38] was representative of this electrocatalyst.

Superior OER performance arising from the composite structure

For the heterogeneous OER process involving gas–liquid–solid three phases, a porous framework, accessible active sites, and an efficient electron-transfer pathway are all highly required for OER catalysts to achieve an excellent performance. In the case of the LDH/oGSH hybrid catalyst, NiFe LDHs primarily served as the OER active phase, while the oGSH substrate not only provided a 3D porous electrical conductive framework, but also effectively regulated the *in situ* LDH growth towards uniform hybridization. It was exactly the synergistic effect of both constituents and the resultant novel structural features that led to the outstanding OER reactivity.

On the one hand, the uniform decoration of dual-sized NiFe LDHs into the nanocarbon framework provided abundant OER active sites and effectively modulated the surface character of the composites. For the 100 nm-sized LDH flakes uniformly dispersed in the hierarchical pores of the nanocarbon framework, they not only dominantly afforded highly active sites, but also served as spacers to prevent the stacking of nanocarbon materials, which further guaranteed smooth gas release and electrolyte permeation. Meanwhile, the 5 nm-sized LDH nanoplates intimately contacted with the nanocarbon underlayer, leading to rapid electron transfer from active phases to the

conductive substrate (as revealed by the impedance measurement in Fig. S8†), and further a strong interfacial coupling effect. Additionally, LDHs with an anion intercalated structure exhibited excellent hydrophilicity. Once introduced into the oGSH substrate, the contact angle of the composites was remarkably decreased (Fig. 3a and S9†), substantially improving the surface wettability and facilitating the permeation of electrolyte ions.

On the other hand, the mesoporous nanocarbon substrate with a specific surface area of 1560 m^2 g^{-1} and a total pore volume of 1.91 cm^3 g^{-1} (Fig. S4†) not only supported and linked up the separated LDH sheets with a highly conductive network of *ca.* 2200 S m^{-1} conductivity (Fig. 3b), but also regulated and controlled the *in situ* growth behaviors of NiFe LDHs. XPS analysis indicated that the surface oxygen content of GSHs was remarkably increased from 1.94 to 4.63 at% after moderate oxidation, introducing a series of oxygen-containing functional groups (quinones, COOH, C=O, C–O, and –OH) (Fig. 3c, S10, and Table S2†). Meanwhile, a considerable amount of defective
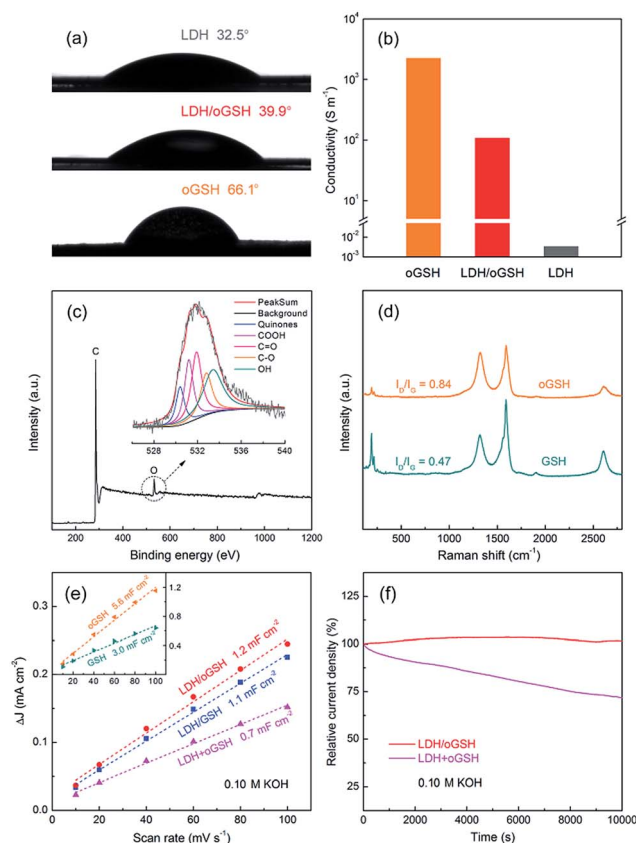

Fig. 3 Enhanced OER performance of LDH/oGSH arising from the *in situ* combination of NiFe LDHs and oxygen-decorated GSHs. (a) Contact angles and (b) electrical conductivities of LDH/oGSH and its individual components. (c) XPS spectrum of oGSHs, and the inset shows the high resolution O 1s spectra. (d) Raman spectra of GSH and oGSH samples. (e) The linear slope of charging current differences plotted against scan rates, equivalent to twice the double-layer capacitance C_{dl}, was used to represent the ECSA. (f) Chronoamperometric response of LDH/oGSH and LDH + oGSH samples at an initial current density of 1.0 mA cm^{-2} in 0.10 M KOH.

This journal is © The Royal Society of Chemistry 2015

J. Mater. Chem. A, 2015, **3**, 24540–24546 | **24543**

sites resulted at the corners and edges of the oGSH layer, as reflected by the increasing intensity ratio of D to G bands in Raman spectra (Fig. 3d). During co-precipitation, both oxygen functionalities and topology-induced defects adsorbed and anchored the metal nitrate precursors, and then the spatially confined NiFe LDH nucleation and growth resulted in uniform decoration of hierarchically structured LDHs into the oGSH skeleton (namely the defect-anchored mechanism), which gave rise to fully exposed active sites and strongly coupled interfacial junctions. Attributed to the binding between NiFe LDHs and oGSHs, the high resolution Ni 2p spectra of the resultant LDH/oGSH exhibited *ca.* 0.9 eV shift to higher binding energy compared with those of LDHs (Fig. S11†), which indicated an effectively modulated local electronic structure of Ni cations. Moreover, compared with that of GSHs, the contact angle of oGSHs was significantly reduced from 131.5 to 66.1° (Fig. S9†), indicating further improved surface wettability and electrolyte penetration due to the mild oxidation. Therefore, both oGSHs and LDH/oGSH exhibited an enhanced OER activity in contrast to their unoxidized counterparts (Fig. 2a), as well as an increasing electrochemically active surface area (ECSA) estimated from the electrochemical double-layer capacitance C_{dl} (Fig. 3e).

Furthermore, resulted from the *in situ* fabrication method, the LDH/oGSH composite delivered both an outstanding OER activity and durability compared with the physical mixture LDH + oGSH. The ECSA of LDH/oGSH was estimated to be *ca.* 70%, higher than that of LDH + oGSH (Fig. 3e), indicating fully exposed and highly accessible active sites due to the *in situ* hybridization. The stability tests at a constant overpotential revealed that the corresponding current density of LDH/oGSH remained almost unchanged after 10 000 s, while only *ca.* 72% of the initial activity was retained for LDH + oGSH (Fig. 3f). This greatly enhanced durability of the LDH/oGSH electrocatalyst was attributed to the strongly coupled interfaces and intimate attachment between NiFe LDHs and oGSHs. The results of catalyst stability evaluated at a moderate initial current density and in a concentrated alkaline solution further verified the durability of LDH/oGSH for OER (Fig. S5b†).

Until now, there have been primarily three different strategies to fabricate the NiFe LDH/nanocarbon hybrids. The first method is the simple solvothermal synthesis in one-pot, that has been reported in NiFe LDH hybridization with CNTs,[29] graphene,[35] and carbon quantum dots.[36] However, the NiFe LDHs hybridized with the substrate randomly and unequally in this procedure, and the nanocarbon materials aggregated and stacked inevitably, which substantially reduced the catalyst porosity and the utilization efficiency of active sites. The second way is using the electrostatic attraction between two oppositely charged nanosheets, namely the exfoliated NiFe LDH plates and the graphene layers.[30,31] Although an alternatively stacked NiFe LDH/graphene structure has been obtained, the step of LDH exfoliation is extremely time-consuming. The final approach is the uniform electrodeposition of nano-sized LDH flakes onto the 3D graphene framework, which was aimed at the fast fabrication of OER electrodes.[33] In this work, we proposed a novel concept of a defect-anchored nucleation and *in situ*

hybridization strategy, through which dual-sized NiFe LDH plates were uniformly and strongly integrated with a self-dispersible graphene/CNT hybrid. The oxygen functionalities and defects on the mildly oxidized carbon substrates anchored the LDH nucleation and *in situ* growth, and further led to a hierarchical porous structure, fully exposed active sites, and strongly coupled interfaces, thereby rendering the composites as an efficient OER catalyst. This family of complexes and the proposed fabrication strategy are expected to open up new avenues for the development of advanced nano-architectured materials for various fields.

3. Conclusions

A novel NiFe LDH/nanocarbon hybrid was proposed and fabricated by incorporating LDH flakes into a self-dispersal carbon framework through defect-anchored nucleation and *in situ* growth. Arising from the synergy of individual components and the unique structural features, the as-fabricated LDH/oGSH electrocatalyst exhibited superior OER performance with a small onset overpotential (*ca.* 240 mV), a low overpotential required for 10 mA cm^{-2} (*ca.* 350 mV), and a decreased Tafel slope (*ca.* 54 mV dec^{-1}) in 0.10 M KOH. The oGSH substrate not only supported NiFe LDH flakes with a mesoporous architecture and an electrical conductive network that facilitated mass diffusion and electron transport, but also modulated the *in situ* growth behavior of LDHs towards a highly uniform and fully accessible arrangement which substantially increased the utilization efficiency of active sites. The dual-sized distribution of *in situ* grown NiFe LDHs gave the composite a porous structure for smooth electrolyte permeation, and introduced adequate intrinsic active sites with a more hydrophilic surface. Furthermore, the defect-anchored nucleation and growth contributed to a strong interaction between the NiFe LDHs and oGSH substrate, thereby stimulating rapid interfacial charge transfer and ensuring enhanced catalyst durability. This work not only provides a promising candidate for OER catalysts, but also inspires the development of new function-phase/nano-carbon composites aimed at various applications, such as heterogeneous catalysis, energy conversion and storage, *etc.*

4. Experimental section

Material synthesis

Oxidation of nanocarbon materials. The GSHs were bulk grown in a fluidized bed reactor through CVD of CH_4. FeMgAl LDH flakes prepared by typical urea assisted co-precipitation were used as the catalysts after *in situ* calcination and reduction in the reactor. The residual catalysts were removed by routine acid (10.0 mol L^{-1} HCl)/alkali (15.0 mol L^{-1} NaOH) treatment for high-purity GSHs. Detailed description of the GSH preparation procedure can be referred to our previous publication.[42] GSHs were mildly oxidized following a modified Hummers' method.[43] 100.0 mg GSHs were first dispersed in 25.0 mL concentrated H_2SO_4. Then, the mixture was transferred into an ice-water bath to maintain its temperature under 10 °C and stirred for 4.0 h. After that, 25.0 mL 10% dilute H_2SO_4 was

24544 | *J. Mater. Chem. A*, 2015, **3**, 24540–24546

This journal is © The Royal Society of Chemistry 2015

gradually added in 1.0 h, followed by slow addition of 75.0 mL deionized water in another 2.0 h. To end the reaction, 2.0 mL H_2O_2 was added into the solution until no gas bubble was released. The oGSH sample was finally obtained after filtering, washing, and freeze-drying.

Synthesis of LDH/oGSH electrocatalysts. The LDH/oGSH catalysts were fabricated through urea assisted co-precipitation with oGSHs as the substrate. Specifically, 50.0 mg oGSHs were dispersed into 40.0 mL N-methylpyrrolidone (NMP) and sonicated for 30 min. Meanwhile, 735.0 mg $Ni(NO_3)_2 \cdot 6H_2O$, 340.0 mg $Fe(NO_3)_3 \cdot 9H_2O$ and 9.0 g urea were dissolved in 50.0 mL deionized water. The as-prepared solution was mixed with the oGSH/NMP suspension, and maintained at 100 °C under continuous magnetic stirring for 6.0 h in a 250.0 mL flask, which was equipped with a reflux condenser in ambient atmosphere. After filtering, washing and freeze-drying, the final product of LDH/oGSH was achieved. In addition, a number of control samples have been prepared. LDH/GSH was fabricated with the pristine GSHs instead of oGSHs under otherwise identical conditions, and bulk LDHs were fabricated without the addition of nanocarbon materials. Through mixing bulk LDHs and oGSHs under sufficient grinding, the LDH + oGSH physical mixture with the same mass composition of LDH/oGSH was also prepared for comparison.

Structural characterization

The morphology and structure of the as-prepared materials were characterized using a JSM 7401F SEM operating at 3.0 kV and a JEM 2010 high resolution TEM operating at 120.0 kV. XRD patterns were recorded on a Bruker D8 Advance diffractometer at 40.0 kV and 120.0 mA with Cu-K$_\alpha$ radiation. XPS measurements were conducted by using an Escalab 250xi. Raman spectra were collected using a Horiba Jobin Yvon LabRAM HR800 Raman spectrophotometer with a He–Ne laser excited at 633 nm. The Brunauer–Emmett–Teller (BET) specific surface area was determined using N_2 adsorption–desorption on an Autosorb-IQ2-MP-C system, and the pore size distribution was computed based on quenched solid density functional theory using the adsorption branch. The composite composition was determined by TGA using a Mettler Toledo TGA/DSC-1 STAR system under an O_2 atmosphere. The contact angle was measured on an OCAH200 optical contact angle measuring instrument. The electrical conductivity was measured using the ST-102A four-probe technique with a Keithley 2636A SourceMeter.

Electrochemical evaluation

Electrochemical tests were carried out on a three-electrode system controlled by using a CHI 760D electrochemistry workstation (CH Instrument, USA) and in O_2-saturated 0.10 or 1.0 M KOH electrolyte. As for the three-electrode system, a rotating disk electrode (RDE, Pine Research Instrument, USA) with a disk diameter of 5.0 mm was used as the substrate for the working electrode, with a Pt sheet and a saturated calomel electrode (SCE) serving as the counter and reference electrodes, respectively. Before each test, the RDE working electrode was fabricated as follows. 5.0 mg electrocatalysts were first dispersed in 0.95 mL ethanol, and then 0.05 mL Nafion solution (5.0 wt%) was added, followed by 1.0 h sonication. 10.0 μL suspension was pipetted onto a glassy carbon disk electrode, which was mechanically polished and ultrasonically washed in advance. Ultimately, the working electrode was prepared after solvent evaporation in air for 10.0 min.

OER performance of the electrocatalysts was evaluated by LSV at a scan rate of 10 mV s^{-1}, with the RDE rotating at 1600 rpm. 95% iR-compensation was applied during all LSV and chronoamperometric tests. The overpotential η was calculated as $\eta = E_{vs.~SCE} + 0.0592$ pH $+ 0.241 - 1.229$. In general, these electrochemical tests exhibited satisfactory repeatability (Fig. S12†). To decouple the currents of catalyst oxidation and oxygen evolution, the chronoamperometric method with a constant potential being exerted on the working electrode was used. The catalyst oxidation current faded away quickly in a few seconds, and then the current approached a constant value over time, which is ascribed to the OER current at the corresponding potential. By varying the exerted potential over a suitable range, the correspondence between OER current and overpotential was obtained, and these voltammetry curves could substitute LSV plots to approximate the onset potential. The electrochemical impedance spectroscopy measurement was performed at 0.52 V vs. SCE over a frequency range from 10 mHz to 10 kHz at a sinusoidal voltage amplitude of 5.0 mV. The catalyst stability was tested at a constant overpotential required to reach an initial current density of 1.0 or 5.0 mA cm^{-2}.

The ECSA was determined by measuring the capacitive current associated with double-layer charging from the scan-rate dependence of cyclic voltammetry. This measurement was performed on the same working electrode within a potential window of 0–50 mV vs. SCE and scan rates ranging from 10 to 100 mV s^{-1}. Then linear fitting of the charging current density differences ($\Delta j = j_a - j_c$ at the potential of 25 mV vs. SCE) against the scan rate was carried out. The slope was twice of the double-layer capacitance C_{dl}, which was used to represent the ECSA.

The faradaic efficiency of the catalyst sample for OER was tested using a rotating ring disk electrode (RRDE) in N_2-saturated 0.10 M KOH solution. Before the test, the catalyst sample was deposited on the disk electrode through the same preparation method as that for the RDE. Then, the disk electrode rotating at 1600 rpm was sequentially subjected to a series of overpotentials of 0.300, 0.302, 0.304, 0.306, 0.308, 0.310, and 0.312 V, while the ring electrode was held constant at 0.37 V vs. reversible hydrogen electrode (RHE). With both the disk and ring corresponding currents being recorded, the faradaic efficiency can be determined as $(n_{app} \times i_r)/(i_d \times N)$. Here, n_{app} is the apparent number of electrons, which was reported to be 2 at 1600 rpm rotating speed;[44] i_r and i_d are respectively the measured ring and disk current densities and N is the collection efficiency of the Pt ring, which was determined to be 0.26 based on our previous work.[38]

Acknowledgements

Notes and references

1 H. B. Gray, *Nat. Chem.*, 2009, **1**, 7.
2 A. Kudo and Y. Miseki, *Chem. Soc. Rev.*, 2009, **38**, 253.
3 J. A. Turner, *Science*, 2004, **305**, 972.
4 M. G. Walter, E. L. Warren, J. R. McKone, S. W. Boettcher, Q. Mi, E. A. Santori and N. S. Lewis, *Chem. Rev.*, 2010, **110**, 6446.
5 H. Wang, Y. Yang, Y. Liang, G. Zheng, Y. Li, Y. Cui and H. Dai, *Energy Environ. Sci.*, 2012, **5**, 7931.
6 Y. Jiao, Y. Zheng, M. Jaroniec and S. Z. Qiao, *Chem. Soc. Rev.*, 2015, **44**, 2060.
7 M. T. Koper, *J. Electroanal. Chem.*, 2011, **660**, 254.
8 Y. Lee, J. Suntivich, K. J. May, E. E. Perry and Y. Shao-Horn, *J. Phys. Chem. Lett.*, 2012, **3**, 399.
9 D. Galizzioli, F. Tantardini and S. Trasatti, *J. Appl. Electrochem.*, 1974, **4**, 57.
10 J. Wang, H. X. Zhong, Y. l. Qin and X. B. Zhang, *Angew. Chem., Int. Ed.*, 2013, **52**, 5248.
11 M. Zhang, M. de Respinis and H. Frei, *Nat. Chem.*, 2014, **6**, 362.
12 Z. Zhao, H. Wu, H. He, X. Xu and Y. Jin, *Adv. Funct. Mater.*, 2014, **24**, 4698.
13 J. Wang, T. Qiu, X. Chen, Y. Lu and W. Yang, *J. Power Sources*, 2014, **268**, 341.
14 M. W. Louie and A. T. Bell, *J. Am. Chem. Soc.*, 2013, **135**, 12329.
15 Y.-F. Li and A. Selloni, *ACS Catal.*, 2014, **4**, 1148.
16 M. S. Burke, M. G. Kast, L. Trotochaud, A. M. Smith and S. W. Boettcher, *J. Am. Chem. Soc.*, 2015, **137**, 3638.
17 Y. Zhu, W. Zhou, Z. G. Chen, Y. Chen, C. Su, M. O. Tadé and Z. Shao, *Angew. Chem., Int. Ed.*, 2015, **54**, 3897.
18 F. Song and X. Hu, *J. Am. Chem. Soc.*, 2014, **136**, 16481.
19 R. Subbaraman, D. Tripkovic, K.-C. Chang, D. Strmcnik, A. P. Paulikas, P. Hirunsit, M. Chan, J. Greeley, V. Stamenkovic and N. M. Markovic, *Nat. Mater.*, 2012, **11**, 550.
20 R. D. Smith, M. S. Prévot, R. D. Fagan, S. Trudel and C. P. Berlinguette, *J. Am. Chem. Soc.*, 2013, **135**, 11580.
21 S. Ci, S. Mao, Y. Hou, S. Cui, H. Kim, R. Ren, Z. Wen and J. Chen, *J. Mater. Chem. A*, 2015, **3**, 7986.
22 J. Luo, J.-H. Im, M. T. Mayer, M. Schreier, M. K. Nazeeruddin, N.-G. Park, S. D. Tilley, H. J. Fan and M. Grätzel, *Science*, 2014, **345**, 1593.
23 F. Song and X. Hu, *Nat. Commun.*, 2014, **5**, 4477.
24 X. Lu and C. Zhao, *Nat. Commun.*, 2015, **6**, 6616.
25 M. Gong and H. Dai, *Nano Res.*, 2015, **8**, 23.
26 Z. Lu, W. Xu, W. Zhu, Q. Yang, X. Lei, J. Liu, Y. Li, X. Sun and X. Duan, *Chem. Commun.*, 2014, **50**, 6479.
27 L. Qian, Z. Lu, T. Xu, X. Wu, Y. Tian, Y. Li, Z. Huo, X. Sun and X. Duan, *Adv. Energy Mater.*, 2015, **5**, 1500245.
28 Z. Li, M. Shao, H. An, Z. Wang, S. Xu, M. Wei, D. G. Evans and X. Duan, *Chem. Sci.*, 2015, **6**, 6624.
29 M. Gong, Y. Li, H. Wang, Y. Liang, J. Z. Wu, J. Zhou, J. Wang, T. Regier, F. Wei and H. Dai, *J. Am. Chem. Soc.*, 2013, **135**, 8452.
30 X. Long, J. Li, S. Xiao, K. Yan, Z. Wang, H. Chen and S. Yang, *Angew. Chem., Int. Ed.*, 2014, **126**, 7714.
31 W. Ma, R. Ma, C. Wang, J. Liang, X. Liu, K. Zhou and T. Sasaki, *ACS Nano*, 2015, **9**, 1977.
32 C. Tang, H. S. Wang, H. F. Wang, Q. Zhang, G. L. Tian, J. Q. Nie and F. Wei, *Adv. Mater.*, 2015, **27**, 4516.
33 X. Yu, M. Zhang, W. Yuan and G. Shi, *J. Mater. Chem. A*, 2015, **3**, 6921.
34 H.-F. Wang, C. Tang and Q. Zhang, *J. Mater. Chem. A*, 2015, **3**, 16183.
35 D. H. Youn, Y. B. Park, J. Y. Kim, G. Magesh, Y. J. Jang and J. S. Lee, *J. Power Sources*, 2015, **294**, 437.
36 D. Tang, J. Liu, X. Wu, R. Liu, X. Han, Y. Han, H. Huang, Y. Liu and Z. Kang, *ACS Appl. Mater. Interfaces*, 2014, **6**, 7918.
37 M.-Q. Zhao, X.-F. Liu, Q. Zhang, G.-L. Tian, J.-Q. Huang, W. Zhu and F. Wei, *ACS Nano*, 2012, **6**, 10759.
38 G.-L. Tian, M.-Q. Zhao, D. Yu, X.-Y. Kong, J.-Q. Huang, Q. Zhang and F. Wei, *Small*, 2014, **10**, 2251.
39 W. Zhou, X. Bai, E. Wang and S. Xie, *Adv. Mater.*, 2009, **21**, 4565.
40 Q. Zhang, J. Q. Huang, M. Q. Zhao, W. Z. Qian and F. Wei, *ChemSusChem*, 2011, **4**, 864.
41 M.-Q. Zhao, Q. Zhang, J.-Q. Huang, G.-L. Tian, T.-C. Chen, W.-Z. Qian and F. Wei, *Carbon*, 2013, **54**, 403.
42 M.-Q. Zhao, H.-J. Peng, Q. Zhang, J.-Q. Huang, G.-L. Tian, C. Tang, L. Hu, H.-R. Jiang, H.-Y. Cai, H.-X. Yuan and F. Wei, *Carbon*, 2014, **67**, 554.
43 W. S. Hummers Jr and R. E. Offeman, *J. Am. Chem. Soc.*, 1958, **80**, 1339.
44 C. C. McCrory, S. Jung, J. C. Peters and T. F. Jaramillo, *J. Am. Chem. Soc.*, 2013, **135**, 16977.
45 X. Lu, W.-L. Yim, B. H. Suryanto and C. Zhao, *J. Am. Chem. Soc.*, 2015, **137**, 2901.
46 D. Friebel, M. W. Louie, M. Bajdich, K. E. Sanwald, Y. Cai, A. M. Wise, M.-J. Cheng, D. Sokaras, T.-C. Weng and R. Alonso-Mori, *J. Am. Chem. Soc.*, 2015, **137**, 1305.
47 L. Trotochaud, S. L. Young, J. K. Ranney and S. W. Boettcher, *J. Am. Chem. Soc.*, 2014, **136**, 6744.

24546 | *J. Mater. Chem. A*, 2015, **3**, 24540–24546

This journal is © The Royal Society of Chemistry 2015